FNAL-PUB-08-507-APC

Observation and Simulation of Space-Charge Effects in a Radio-Frequency Photoinjector using a Transverse Multi-beamlet Distribution

M. Rihaoui,[1, 2] P. Piot,[1, 3] J. G. Power,[2] Z. Yusof,[2] and W. Gai[2]

[1]*Northern Illinois Center for Accelerator & Detector Development and Department of Physics, Northern Illinois University, DeKalb IL 60115, USA*
[2]*High Energy Physics Division, Argonne National Laboratory, Argonne IL 60439, USA*
[3]*Accelerator Physics Center, Fermi National Accelerator Laboratory, Batavia, IL 60510, USA*

(Dated: April 20, 2009)

We report on a new experimental study of the space-charge effect in a radio-frequency (rf) photoinjector. A 5 MeV electron bunch, consisting of a number of beamlets separated transversely, was generated in an rf photocathode gun and propagated in the succeeding drift space. The collective interaction of these beamlets was studied for different experimental conditions. The experiment allowed the exploration of space-charge effects and its comparison with 3D particle-in-cell simulations. Our observations also suggest the possible use of a multi-beam configuration to tailor the transverse distribution of an electron beam

PACS numbers: 29.27.-a, 41.85.-p, 41.75.Fr

I. INTRODUCTION

Many accelerator applications call for the production of high charge (few nC), low transverse emittance (few μm), high peak current (several kA) electron bunches. Such applications range from accelerator-based light sources [1] and high energy physics accelerators [2] to novel acceleration techniques, e.g., based on dielectric wakefield accelerators [3]. The dynamics of such very bright, space-charge dominated, electron beams is intricate: it can develop transverse instabilities and is subject to phase space diluting effects [4, 5]. Typically, high-brightness electron bunches are produced in a photoinjector: a high quantum efficiency photocathode, illuminated by a laser, is located on the back plate of a radio-frequency (rf) resonant cavity. High-charge bunches are photoemitted and rapidly accelerated to relativistic energies [6] and the electron bunch properties are strongly affected by the photocathode drive laser parameters.

Several theoretical and experimental studies have previously addressed detrimental effects due to an inhomogeneous initial distribution in a rf photoinjector, e.g., photocathode drive laser transverse distribution non-uniformities. In most investigations, the beam is statistically characterized using its rms properties. For instance Reference [7] experimentally explores the impact of transverse modulation on the root-mean-square (rms) transverse emittance. Although this is a universal characterization relying on the concept of "equivalent beam" [8, 9] important details of the beam evolution might be missed. The pioneering work of Reiser and co-workers underlined the importance of studying the evolution of the beams transverse distribution and not only its rms properties [10, 11]. Our experiment used a quincunx pattern to generate five beamlets separated transversely. In this paper, we present a similar experiment performed in an rf photoinjector using a ~ 5 MeV bunched electron beam.

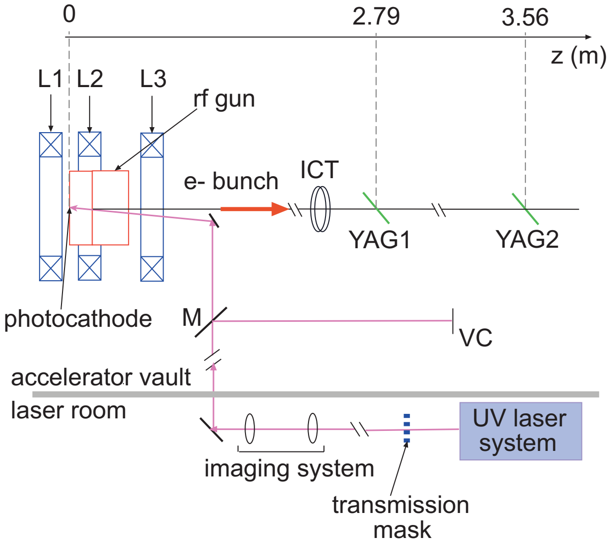

FIG. 1: (Color) Overview of the AWA beam line. Here, only the elements pertaining to our experiment are shown. The legend represents solenoidal magnetic lenses (L), optical mirror (M), virtual cathode (VC), integrated current monitor (ICT), and transverse profile monitor (YAG1 and 2). The distance along the beamline is also shown.

Masking the transverse distribution of the photocathode drive-laser allowed the generation of a beam that consisted of several beamlets separated transversely. The evolution of the beamlets transverse density provides information on transverse space charge effects which are validated against particle-in-cell (PIC) simulations. Furthermore, our experimental observations hint to a possible use of multi-beamlet configuration to transversely control a beam. This could open new ways of manipulating an electron beam using space charge interaction between several beams in a photoinjector. Several schemes based on space charge interaction have been proposed as ways to control or shape charged-particle beams. For instance Reference [12] discusses the design of a very fast kicker based on such a scheme. Similarly, a technique using an electron lens to compensate tune shift induced by beam-beam effects in circular colliders was recently demonstrated in the Tevatron collider at Fermilab [13].

II. EXPERIMENTAL SETUP

The experiment was performed at the Argonne Wakefield Accelerator (AWA) [14]; see Fig. 1. The accelerator incorporates a photoemission source consisting of a 1+1/2 cell rf cavity operating at $f = 1.3$ GHz, henceforth referred to as rf gun. An ultraviolet (uv) laser beam impinges a magnesium photocathode located on the back plate of the rf gun half cell. The thereby photoemitted electron bunch exits from the rf gun with a maximum kinetic energy of approximately 5 MeV and is allowed to drift for few meters with no external field save for the solenoid magnets. Two 100 micron thick Ce:YAG screens [15] are used to measure the beams transverse distribution. An integrated current monitor [16] provides the charge per bunch. The uv laser system consists of a Titanium Sapphire laser amplified with a regenerative amplifier and two linear amplifiers [17]. The infrared laser is frequency-tripled to $\lambda = 248$ nm and can be further amplified in a single-stage Krypton Fluoride excimer amplifier. The laser system is located ∼20 m from the photocathode and the laser beam is transported via an optical imaging system.

The rf gun is surrounded by three solenoidal magnetic lenses independently powered referred to as L1, L2 and L3; see Fig. 1. During the experiment reported here only L3 was used. The transverse distribution of the uv laser on the photocathode can be measured from a duplicate image of the laser beam on a “virtual photocathode.” The virtual photocathode consists of a uv sensitive CCD camera, located outside of the vacuum chamber, and is a one-to-one optical image of the laser on the photocathode.

The transverse distribution on the photocathode was controlled with a mask, located in the object plane of the imaging system, with a series of identical holes that could be selectively blocked (see Fig. 2). This object plane is located in the laser room thereby allowing laser shaping without interrupting the accelerator operation. The mask's center-to-center hole separation is 2 mm and the hole diameter is 1 mm. The uv laser beam temporal profile was measured with a streak camera and can be approximated by a Gaussian distribution with rms duration of $\sigma_t \simeq 2$ ps.

III. EXPERIMENTAL RESULTS & COMPUTER SIMULATIONS

A. Low charge regime

The operating conditions of the main subsystems of the photoinjector, used during the experiment reported herein, are gathered in Table I. The first experiment consisted in generating a low charge electron beam comprising six beamlets (Fig. 3) arranged in an assymetric pattern. This enabled us to identify the orientation of the pattern on both the virtual cathode and YAG1. Due to low space charge effects, the beamlets do not interact strongly and effectively behave as independent macroparticles. The observed pattern rotation between the photocathode and YAG1 , visible in Fig. 3 results from the Larmor precession induced as the beam propagates through the L3 magnetic lens. The rotation angle is given by [18]:

$$\theta(z) = \int_0^z [eB(r=0,z)]/[2m\gamma(z)\beta(z)c]dz \qquad (1)$$

where $B(r=0,z)$ is the axial component of magnetic field experienced by the beam, $\gamma(z)$ the beam's Lorentz factor and $\beta(z) \equiv [1-\gamma(z)^{-2}]^{1/2}$. The rotation angle downstream of the solenoid field, $\theta(\infty)$, was calculated by numerically integrating Eq. 1 using the axial magnetic field obtained from Poisson [19] while $\beta(z)$ was computed with Impact-T [20]. The calculated rotation angle downstream of the solenoidal field was found to be $\theta(\infty) = -32 \pm 2$ deg (the quoted uncertainty comes from the uncertainty on the peak E-field in the rf gun). The computed value compares well with the measured roration angle of $\theta(\infty) = -34.7 \pm 2.6$ deg for a peak axial magnetic field $\hat{B} = 0.339$ T.

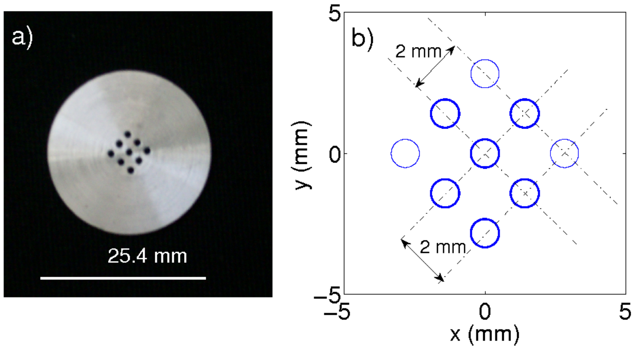

FIG. 2: Picture (a) of the aluminum mask used to shape the laser beam into a series of transversely-separated beamlets and corresponding closeup of the mask geometry (b). In the experiments reported in this paper only five or six holes were not obstructed [show as thicker line circles in (b)] and the mask was oriented to yield the pattern shown in (b) on the virtual photocathode [see also Fig. 3 (left image) for the corresponding uv laser transverse density].

TABLE I: Nominal accelerator settings during the experiment. The "Experiment" and "Model" columns respectively correspond to values inferred from the AWA control system and values obtained when matching the impact-T model to the single particle measurements.

Parameter (unit)	Experiment	Model
Laser rms pulse duration (ps)	1.9 ± 0.2	1.9
laser injection phase (deg)	50 ± 5	53
E-field on cathode (MV/m)	54 ± 3	51
L3 peak axial B-field (T)	$[0.30, 0.40] \pm 0.01$	[0.30,0.40]
Charge - high charge (nC)	0.9 ± 0.1	0.9
Charge - low charge (nC)	0.015 ± 0.005	0.015
Kinetic Energy (MeV)	5.20 ± 0.10	5.28

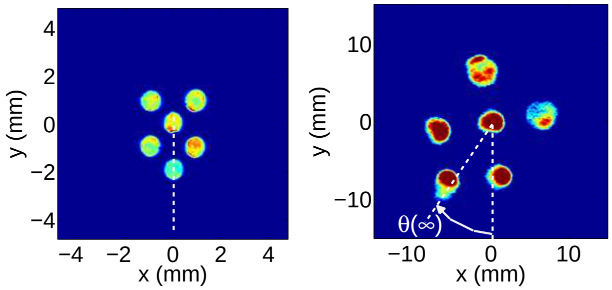

FIG. 3: (Color) False color image of the measured uv laser transverse distribution on the virtual cathode (VC) location (left) and corresponding measured electron beam distribution at YAG1 location (right). The charge is $Q = 20 \pm 2$ pC.

To aid in understanding the experiment, we performed 3D PIC simulations of the beam dynamics using the program Impact-T. The code uses the electrostatic space charge routine where the force is found by solving Poissons equation in the bunch's rest frame [20]. Impact-T was run with a simplex optimizer [21] to fine tune the operating parameters of the accelerator used in the model to match the low charge measurements. During the optimization process the E-field on the cathode, laser injection phase and L3 peak axial B-field were varied to insure the simulation of a low charge quincunx pattern reproduces the low charge measurement on YAG1 (shown in Fig. 3). The minimization criterion for the optimization was to match the measured and simulated positions of the beamlets' centroid. The set of parameters obtained are compiled in Table I and are in good agreement with the settings inferred from the accelerator control system.

B. High charge regime

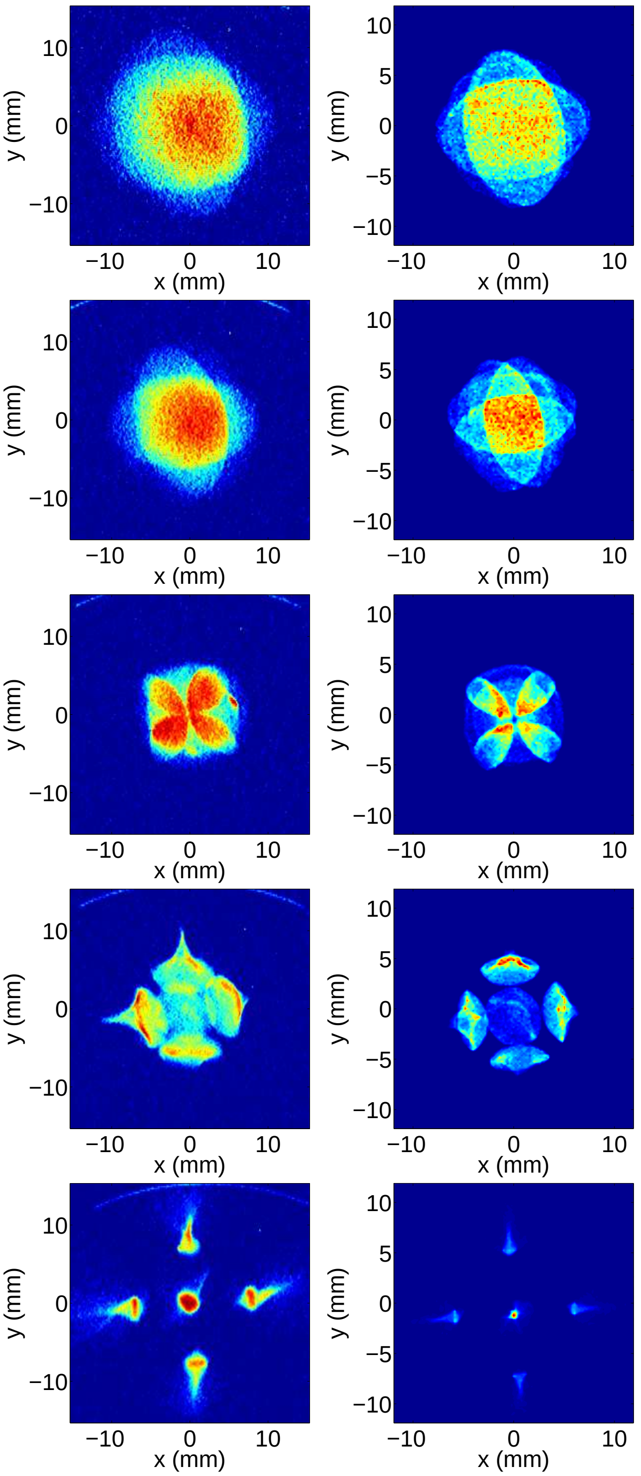

FIG. 4: (Color) False color images of the measured (left column) and simulated (right column) electron beam transverse density distribution at YAG1 location. The five row respectively correspond to different values of the magnetic field (from top row) $\hat{B}$ =0.333, 0.339, 0.350, 0.359, 0.376 T.

At high charge fully 3D codes are necessary to accurately simulate the propagation the non-cylindrically-symmetric distributions considered in this paper. The initial 3D spatial distribution of macroparticles used in our numerical simulations were generated with a quasi-random generator using the digitized pictures of the laser transverse density captured on the virtual cathode. The algorithm, presented in the appendix A, can also be used to generate a temporal distribution based on a measured profile (from a streak camera for example). However, in this experiment the laser was assumed to have a Gaussian temporal distribution with a measured rms duration of 2 ps. The corresponding initial momentum distribution of the macroparticles was generated to follow an isotropic distribution in the forward half-sphere. The momentum modulus of each macroparticle is computed from the excess kinetic energy taken to be 1 eV in the present case. As the total charge associated with the multibeamlet distribution is increased to ∼ 1 nC, space charge becomes significant resulting in a change in: (1) intra-dynamics within the beamlets and (2) interactions between the beamlets. Such interactions resulted in the development of unexpected features that depend on the initial pattern [22]. In Fig. 4, we present the measured and simulated transverse distributions at YAG1 for different values of the L3 magnetic fields $\hat{B}$. The simulations reproduce the main features observed experimentally, especially the formation of radial tails on the periphery of the beamlets. For large values of the magnetic field the central beamlet appears confined. This focusing effect resulting from the presence of the peripheral beamlets is confirmed by masking the surrounding beamlets: the central beamlet rms transverse beam size increases from 1.1 ± 0.3 mm to 3.9 ± 0.3 mm; see Fig. 5.

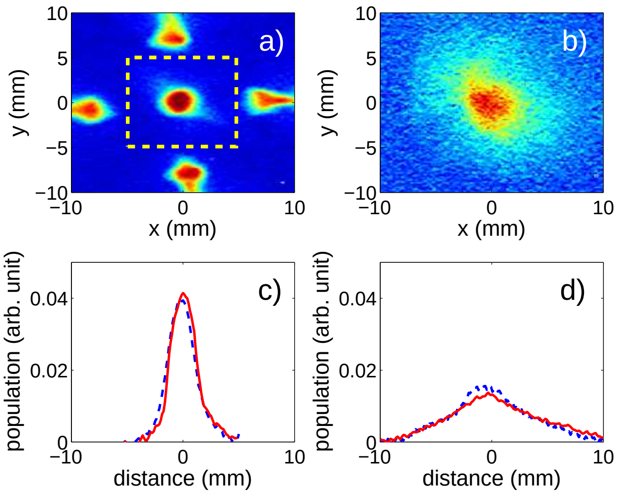

FIG. 5: (Color) measured two-dimensional transverse beam density at YAG1 location and corresponding horizontal (blue dashed line) and vertical (red solid line) projections for the cases with [$Q = 0.93 \pm 0.05$ nC] (a,c) and without (b,d) [$Q = 0.17 \pm 0.03$ nC] surrounding beamlets. The dashed box in (a) represents the region of interest used to compute the projection displayed in (d).

IV. ANALYSIS

Given the reasonable agreement between simulations and measurements shown in the preceding sections, it remains to be understood the origin of the observed features. The primary low charge effect, pattern rotation, has already been shown to be due to the Larmor rotation of the beam upon passing through the solenoidal field. At high charge, there are two notable features that we wish to understand: change in the focusing of the central beamlet and the formation of radial tails on the periphery of the outer beamlets. In this section, we use numerical simulations to provide additional insight into the physical mechanism responsible for these observed features. The initial conditions considered in the present section are similar to the experimental conditions. The only difference is the laser distribution which is now "idealized" by considering the individual beamlets to have a uniform transverse density (instead of using the measured laser distribution). We begin by introducing a rotating coordinate system.

A. Larmor Coordinate System

To simplify the analysis of the simulation results we introduce a rotating coordinate system $\mathbf{\Xi} \equiv (\xi, p_\xi, \zeta, p_\zeta)$ defined as $\mathbf{\Xi}(z) = R[\theta_0 + \theta(z)]\mathbf{X}$ where $\mathbf{X} \equiv (x, p_x, y, p_y)$,

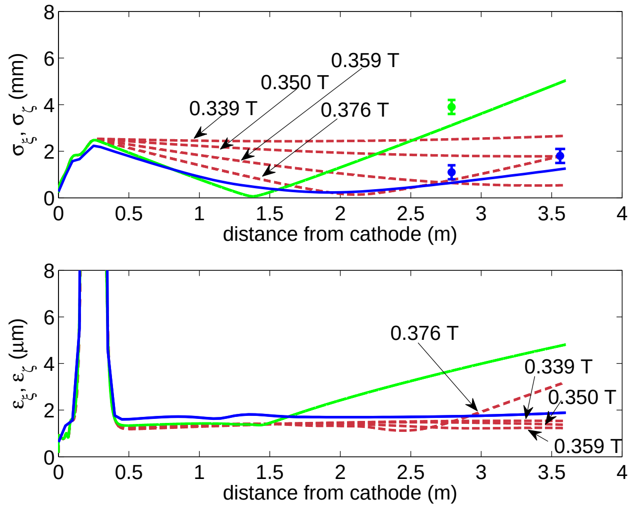

FIG. 6: (Color) Simulations of transverse rms beam size (top) and emittance (bottom) of the central beamlet along the z-axis for different values of L3 peak axial magnetic field $\hat{B} \in [0.339, 0.376]$ T (dashed red lines). The cases shown in Fig. 5 correspond to the blue (with surrounding beamlets) and green (without surrounding beamlets) solid lines. The corresponding data measured at YAG1 and YAG2 are also shown as dots with the same color coding convention as the simulations.

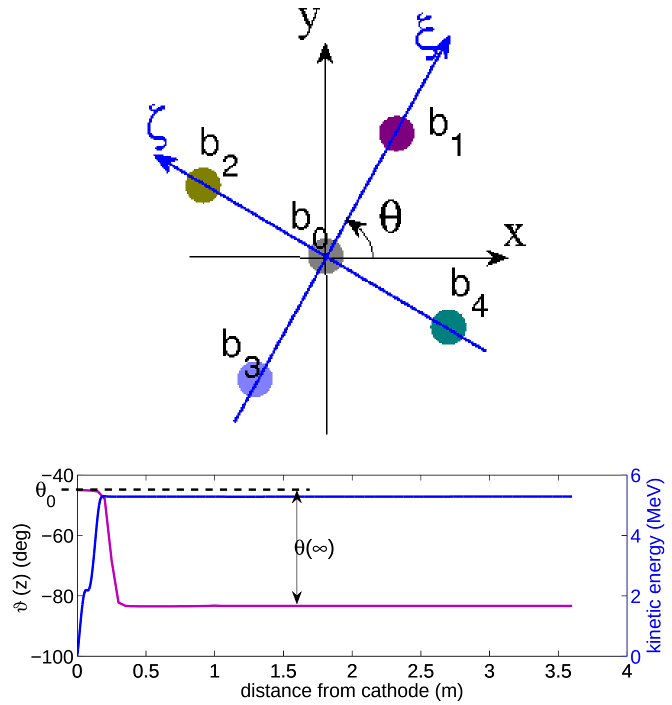

FIG. 7: (Color) Definition of the Larmor (ξ, ζ) and laboratory (x, y) transverse coordinate systems (top schematics). Evolution of the rotation angle $\vartheta(z) \equiv \theta_0 + \theta(z)$ between the (x, y) and Larmor (ξ, ζ) frames (magenta trace) and of the beam's kinetic energy (blue trace) along the accelerator beamline for $\hat{B} = 0.376$ T (bottom plot). In this example $\theta_0 = -45°$ and $\theta(\infty) \simeq -38°$.

θ_0 and $\theta(z)$ are respectively the initial rotation angle of the quincunx pattern on the photocathode and the Larmor rotation angle, and R is a four-dimensional rotation matrix,

$$R[\vartheta(z)] = \begin{bmatrix} I\cos\vartheta(z) & I\sin\vartheta(z) \\ -I\sin\vartheta(z) & I\cos\vartheta(z) \end{bmatrix}, \qquad (2)$$

wherein I is 2×2 identity matrix and $\vartheta(z) \equiv \theta(z) + \theta_0$. The angle θ_0 is chosen such that ξ and ζ axes correspond to the two symmetry axes of the quincunx pattern and $\theta(z)$ is numerically computed using Eq. 1; see Fig. 7. The initial pattern rotation angle on the photocathode is $\theta_0 = -45°$. The use of such a Larmor coordinate system avoided dealing with coupling effects between the two transverse degree-of-freedoms. The trajectories and rms transverse envelopes of the five beamlets in the Larmor frame are presented in Fig. 8 for $\hat{B} = 0.376$ T. The beamlets' trajectories intersect at $z \simeq 1.3$ m and the envelopes strongly overlap for $z \leq 1$ m.

B. Space charge focusing of the central beamlet

As discussed in the previous Section, the presence of the peripheral beamlets results in a focusing of the central beamlet at YAG1 location. Once again, this feature is investigated and reproduced via numerical simulations. IMPACT-T calculations performed for various solenoid settings indicate that the surrounding beamlets affect the central beamlet size and transverse emittance

$$\varepsilon_\perp \equiv [\langle(\beta_\perp\gamma)^2\rangle\langle x_\perp^2\rangle - \langle x_\perp(\beta_\perp\gamma)\rangle^2]^{1/2}, \qquad (3)$$

where $x_\perp$ and $\beta_\perp$ are respectively the considered transverse coordinate and the corresponding velocity. This is illustrated in Fig. 6: the case of the central beamlet with surrounding beamlets is the only one that simultaneously maintain a small beam while preserving its transverse emittance almost constant downstream of the rf gun and solenoid (i.e. for $z > 0.5$ m). The resulting focusing at the location of YAG1 is predominantly due to the beamlet interaction upstream of the solenoid. In this region ($z < 0.2$ m in Fig. 5) the presence of the outer beamlet results in a net focusing of the central beamlet which in turn change the net effect of the focusing kick provided by the solenoid. In the case of $\hat{B} = 0.376$ T the central beamlet alone is nominally over focused by the solenoid (green trace in Fig. 5) while the focusing is less (blue trace in Fig. 5) when the peripheral beamlets are present (essentially due to the change of input properties upstream of the solenoid).

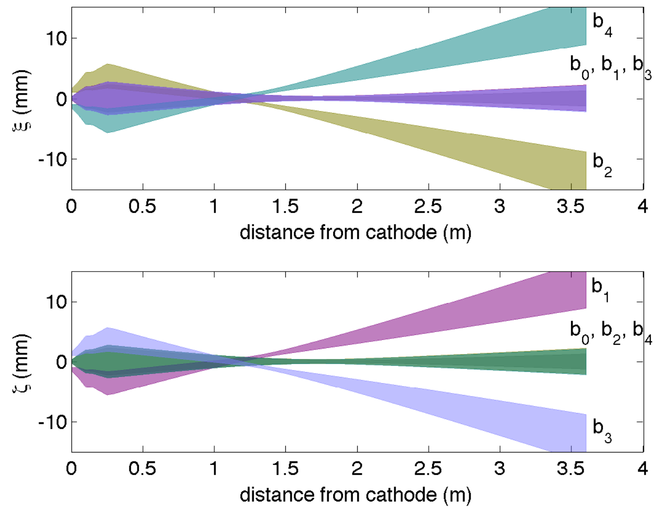

FIG. 8: (Color) Beamlets' transverse rms envelopes and trajectories in the (z, ξ) (top) and (z, ζ) (bottom) for $\hat{B} = 0.376$ T. The B_i labels correspond to the beamlets shown in Fig. 7 (top).

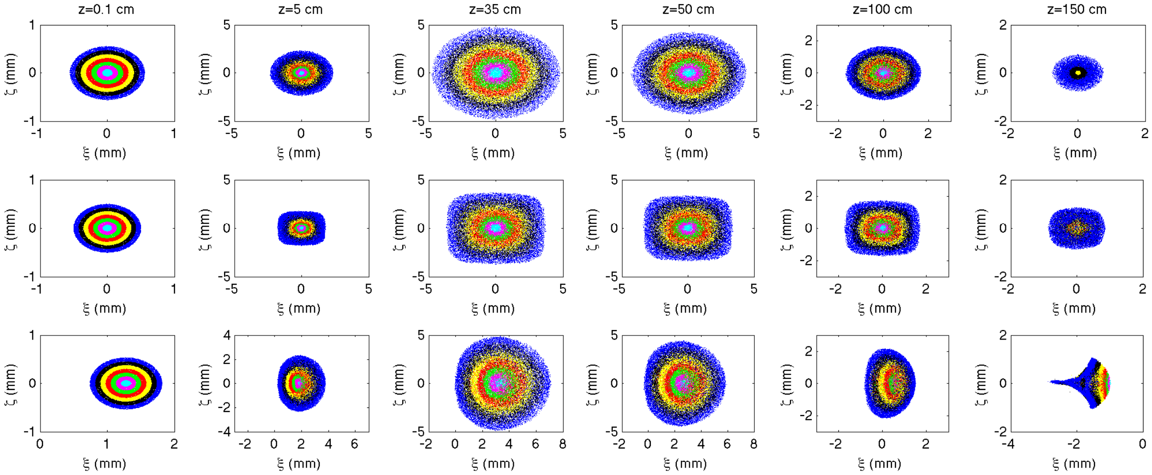

FIG. 9: (Color) Macroparticle distributions in the transverse configuration space at different locations from the photocathode surface ($z = 0.1$, 5, and 35, 50, 100, and 150 cm from left to right columns), for the central beamlet without (top row) and with (middle row) the peripheral beamlets and for the case of one of the peripheral beamlet (bottom row). The peak B-field of L3 is $\hat{B} = 0.376$ T. The coordinate system is the Larmor frame (ξ, ζ). The color coding corresponds to different radial slices at the emission time (the beam at emission was divided into seven radial slices of same thickness $\delta r \simeq 70$ μm).

C. Non-Laminar Flow & Radial Mixing

We now show that transverse space charge is the predominant cause of our observed effects and further insight into the underlying beam dynamics can be inferred from color coding macroparticles according to their initial radial coordinates when photoemitted. Such an analysis is presented in Fig. 9 for the case of the central beamlet {alone (top row) and surrounded by the four peripheral beamlets (middle row)} and for one of the peripheral beamlets (bottom row). The evolution of the transverse configuration space in the Larmor frame (ξ, ζ) shown in the top row of Fig. 9 conforms to the typical evolution of a space-charge-dominated beam in a solenoid and drift space: the radial hierarchy is preserved {a closer examination shows a slight mixing due to (i) the non-uniform (Gaussian) longitudinal distribution of the bunch and (ii) chromatic effects originating from the quadratic dependency of the axial space charge electric field on the radial coordinate [23, 24]} In contrast, the middle row of Fig. 9 presents atypical dynamics: the radial hierarchy is lost and the macroparticles redistribute in the phase space; a large fraction of the beams population crosses over the beamlets central axis. Eventually, the macroparticles retain some degree of organization but the initial radial hierarchy is washed out. The beam transverse distribution is not cylindrically-symmetric. Finally the configuration space associated with one of the peripheral beamlets is shown in the bottom row of Fig. 9. In general, similar remarks as those just mentioned still hold, the main difference being the highly asymmetric distribution. Close inspection of the figure reveals that particles that begin in the outer radial layer of the non-central beamlet near the photocathode, are pushed into the radial tail (blue macroparticles) by space charge as will be shown in the next section.

D. Transverse beam dynamics in the rf gun

Further insight into the mechanism that causes the tail formation can be given by computing the transverse force associated with the density distributions as it propagates along the beamline. We perform such a calculation by numerically solving Poisson's equation in the bunch average rest frame. The thereby obtained scalar potential Φ, tabulated on a three dimensional grid, can directly be used to derive the transverse force a macroparticle would experience as it moves in the laboratory frame [25, 26]. For our purposes, it is more convenient to compute the charge-normalized transverse component of the Lorentz force (in the laboratory frame) a macroparticle with coordinates (ξ, ζ, z) experiences:

$$\mathbf{F}_\perp(\xi, \zeta, z) \simeq \frac{1}{\gamma^2}[\nabla_\perp \Phi](\xi, \zeta, z). \tag{4}$$

where $\nabla_\perp \equiv \hat{\xi}\partial_\xi + \hat{\zeta}\partial_\zeta$ is the transverse gradient. The calculation of $\mathbf{F}_\perp$ was performed numerically in the Larmor frame (ξ, ζ, z). An example of the computed force integrated over the longitudinal bunch distribution, $\mathbf{F}_\perp(\xi, \zeta)$ is shown in Fig. 10 (bottom row) along with the corresponding z-integrated transverse density distributions (top row) for different locations along the accelerator beamline. As can be seen from the force plots, the beamlets begin interacting from their birth, even before overlapping (see $z = 0.1$ cm, Fig. 10). As a result, the transverse force develops a two-fold transverse symmetry. Using the techniques developed in this section we are

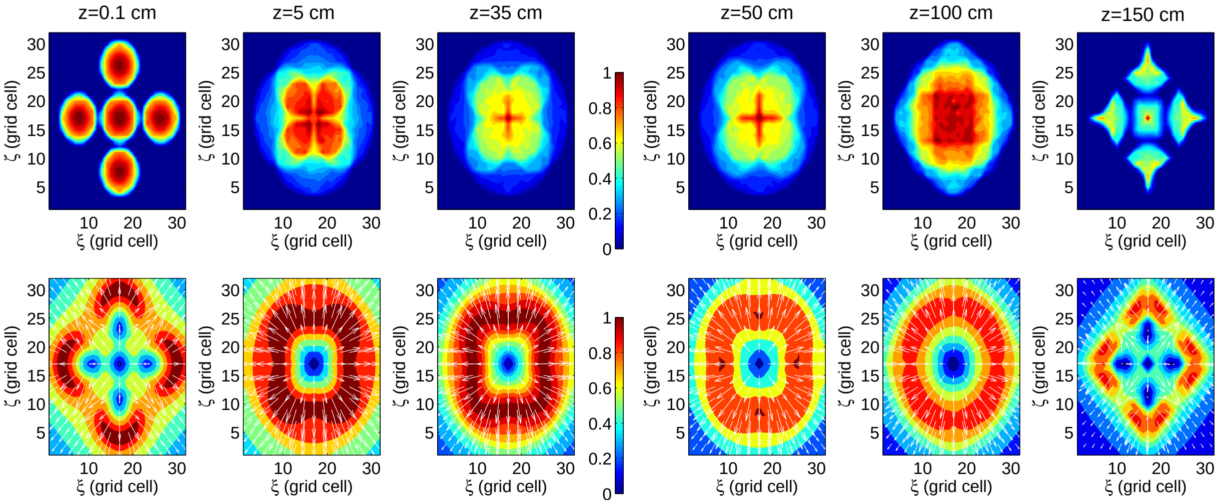

FIG. 10: (Color) z-integrated transverse distribution (top row) and corresponding charge-normalized transverse Lorentz force $\mathbf{F}_{\perp}$ (given by Equation 3) tabulated on a 32×32 transverse grid (bottom rows). The color intensity represents the number of macroparticle (top row) and the force modulus (bottom row). The arrows in the bottom row gives the Lorentz force directions (the arrows length is proportional to the force modulus). Each column corresponds to different position for the bunch center from the photocathode surface (as indicated on the top row) of $z = 0.1$, 5, 35, 50, 100, and 150 cm. The peak B-field of L3 is $\hat{B} = 0.376$ T. The color coding convention for the density (resp. transverse force) is such that blue and red respectively correspond to lowest and largest electron population (resp. force modulus). Note that the plots are in units of the space charge grid cells.

now in a position to understand what causes the formation of the radial tails. Before applying this technique, it was assumed that the tail formation was due to the space charge interaction at the beamlet crossover; approximately $z = 130$ cm. However, we now show that the effect was caused by the space charge interaction at the early stage of the bunch generation and transport. In Fig. 10, it is seen that the space charge force produces a stronger defocusing effect for the population in the outer region of the peripheral beamlets than for the ones in the inner region. While in the rf gun, the beamlets overlap (see Fig. 8 for $z < 0.3$ m) and the thereby produced potential has local minima which results in weaker defocussing forces along four directions (coincident with the two axes of symmetry); see Fig. 10 ($z = 0.5$, 35, and 50 cm). Eventually the beamlets crossover (e.g. $z = 130$ cm) and separate ($z = 150$ cm). Note that the space charge force is nearly axially symmetric at the crossover and therefore incapable of imparting the four-fold symmetry seen in the overall pattern at $z = 150$ cm. The central beamlet becomes square shaped due to the two-fold symmetry of the transverse force while the peripheral beamlets have a one-fold symmetry. The main cause for the largely defocused radial tail containing the inner population of the peripheral beamlets is the transverse force observed earlier (e.g. seen on the $z = 0.1$ cm plot): because of the cross over the electron in the inner region of the peripheral beamlet correspond to electrons initially (before the crossing point) in the outer region.

V. SUMMARY

In summary, we have observed and explained several space-charge induced features associated with a relativistic, multi-beamlet electron bunch. We showed via numerical simulations, that in the quincunx configuration the peripheral beamlets can provide a means to control the transverse size and shape of the central beamlet. Although in the experiment discussed herein we used an external focusing element, a magnetic lens, to force the beamlets trajectories to cross each other and effectively result in the focusing of the central beamlet, one could, in principle, specially design a photoinjector system without an external focusing element. Similarly, using other configurations of surrounding beamlets, one could possibly provide a means for tailoring the bunch transverse distribution. The technique discussed here might be applicable to electron sources based on superconducting rf guns, where the use of an external magnetic field to focus (or shape) the beam can be difficult. Finally, the possibility to focus a beam using a photoemitted electron beam with a temporal profile different from the main beam might also open new ways of controlling the evolution of transverse emittance associated to space-charge-dominated electron beams [27, 28].

VI. ACKNOWLEDGMENT

We are grateful to Dr. Ji Qiang from Lawrence Berkeley National Laboratory for providing us with a copy of

Impact-T. The work of M.R. and P.P. was supported by the US Department of Energy under Contracts No. DE-FG02-04ER41323 and DE-FG02-08ER41532 with Northern Illinois University. W.G., J.P., and Z.Y. are supported by the U.S. Department of Energy under Contract No. DE-AC02-06CH11357 with Argonne National Laboratory.

APPENDIX A: MEASUREMENT-BASED GENERATIONS OF 3D MACROPARTICLE DISTRIBUTIONS

A Monte-Carlo generator was developed to generate an initial 3D macroparticle distribution of N macroparticles, $\{x_k, y_k, t_k\}$ where $k \in [1, N]$, at the photocathode based on the measured laser distribution. The laser distribution was assumed to be factorizable into separate transverse $\mathcal{I}(x, y)$ and temporal $\mathcal{S}(t)$ distributions. The laser transverse distribution can be measured by digitizing the laser spot image on the virtual cathode; see Fig. 1. Given a typical 8-bit CCD camera, with a 640×480 pixel array, the measurement results in a matrix of pixel values $I_{i,j}$ where $i = [1, 2, ..., 640]$, $j = [1, 2, ..., 480]$ and $0 \leq I_{i,j} \leq 255$. The measured temporal distribution (measured with a streak camera in our case) results in a vector S_q with q running over the number of pixels used in the measurement.

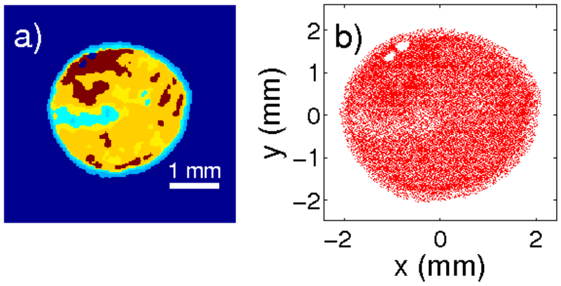

FIG. 11: (Color) Example of measured transverse laser intensity distribution (a) and corresponding generated macroparticle distribution (b). Note that only 20000 macroparticle are displayed for clarity.

The generation of the transverse macroparticle distribution, $\{x_k, y_k\}$ with $k = 1..N$, proceeds as follows. The measured raw image $I_{i,j}$ is processed median filter is applied to remove salt and pepper noise, a background image (i.e. an image without laser beam present) can be subtracted and a threshold applied (i.e. the image elements below a user-defined value are zeroed). Finally a region-of-interest can be selected. The thereby obtained matrix, $I_{i,j}$, with its values normalized such that $\max[I_{i,j}] = 1$, is then used as the discretized density function (the maximum size of the array is 640×480 corresponding to the CCDs pixel array). in the following Monte-Carlo algorithm:

1. A triplet of real random numbers (x, y, J) uniformly distributed in the respective intervals $x \in [0, 639]$, $y \in [0, 479]$, and $J \in [0, 1]$ is generated. We used the Sobol sequence [29] to generate the quasi-random sequence of numbers to achieve more uniformly spaced samples of triplets.

2. If the condition $I[\text{round}(x), \text{round}(y)] > J$, then the triplet is considered valid and a macroparticle with transverse coordinates (x, y) is added to the initial distribution.

3. If the aforementioned condition is not fulfilled, then the (x, y, J) triplet is rejected and step 1 is repeated

4. Steps 1, 2, and 3 are repeated until N macroparticles are generated.

Finally the coordinates of the macroparticles are scaled per the calibration of the CCD camera measurement. An example of the measured image along with the associated macroparticle transverse distributions generated with the above algorithm is presented in Fig. 11.

Similarly, the measured and processed 1D temporal distribution, S_q, can be used to generated the longitudinal coordinates of the macroparticles. However because of the Gaussian temporal shape of the laser pulse we used the measured rms duration σ_t to directly generate time coordinates that have a Normal distribution using the Box-Muller [30] transformation: two independent real variables u and v randomly distributed in $[0, 1]$ are combined to generate the coordinate t_i via

$$t_i = \sigma_t \sqrt{-2 \log u_i} \cos(2\pi v_i). \tag{5}$$

---

[1] see for instance: LCLS Conceptual design report, report SLAC-R-593/UC-414, SLAC (2002); TESLA Technical design report Imprint No. DESY 2001-011 or ECFA 2001-209 (2001).

[2] see the word wide website `http://www.linearcollider.org`.

[3] W. Gai, P. Schoessow, B. Cole, R. Konecny, J. Norem, J. Rosenzweig, and J. Simpson, *Phys. Rev. Lett.* **61**, 2765 (1988).

[4] R. L. Gluckstern, *Phys. Rev. Lett.* **73**, 1247 (1994).

[5] S. Bernal, R.A. Kishek, M. Reiser, in *Proceedings of the 1999 Particle Accelerator Conference* (New-York), 1749 (1999).

[6] J.S. Fraser, R.L. Scheffield, E.R. Gray, and G.W. Ro-

denz, in *Proceedings of the 1985 IEEE Particle Accelerator Conference* (Vancouver, BC), 1791 (1985).

[7] F. Zhou, I. Ben-Zvi, M. Babzien, X. Y. Chang, A. Doyuran, R. Malone, X. J. Wang and V. Yakimenko, *Phys. Rev. ST Accel. Beams* **5**, 094203 (2002).

[8] C. Lejeune and J. Aubert, *Adv. Electron. Electron Phys. Suppl.* **A 13**, 159 (1980).

[9] F. R. Sacherrer, *IEEE Trans. Nucl. Sci.*, **NS-18**, 1105 (1971).

[10] M. Reiser *et al.*, *Phys. Rev. Lett.* **61**, 2933 (1988).

[11] I. Haber, *et al.*, Phys. Rev. A. **44**, 8 (1991).

[12] V. Shiltsev, *Nucl. Intrum. Method*, **A 374**, 137 (1996).

[13] V. Shiltsev, et al., *Phys. Rev. ST Accel. Beams* **11**, 103501 (2008).

[14] information on the Argonne Wakefield Facility are available at the word wide website `http://gate.hep.anl.gov/awa`.

[15] The Ce:YAG screens were procured from Crytur Ltd.; see the word wide website at `http://www.crytur.cz/`

[16] The ICT is manufactured by Bergoz Instrumentation; see the word wide website at `http://www.bergoz.com/`

[17] J.G. Power, H. Wang, M.E. Conde, W. Gai, R. Konecny, W. Liu, Z. Yusof, "Transverse beam envelope measurements and the limitations of the 3-screen emittance method for space-charge dominated beams," *Nucl. Intrum. Method*, **A 546**, 345 (2005).

[18] M. Reiser *The Theory and design of Charged Particle Beams*, Wiley series in beam physics and accelerator technology, Edited by John Wiley & Sons, Inc. (1994); see Equation 3.59 p 74.

[19] J. H. Billen and L. M. Young, in *Proceedings of the 1993 Particle Accelerator Conference*, Washington DC (IEEE, Piscataway, NJ, 1993), 790792 (1993).

[20] J. Qiang, S. Lidia, R. D. Ryne and C. Limborg-Deprey, *Phys. Rev. ST Accel. Beams* **9**, 044204 (2006).

[21] H. Shang, and M. Borland, in *Proceedings of 2005 Particle Accelerator Conference*, Knoxville, Tennessee , 4230 (2005).

[22] M. Rihaoui, W. Gai, P. Piot, J. Power, Z. Yusof, "Measurement of transverse space charge effects in a mutlibeamlet electron bunch produced in a photo-emission electron source," to be presented at the 2009 Particle Accelerator Conference.

[23] G. Geloni, E. Saldin, E. Schneidmiller, and M. Yurkov, *Nucl. Instrum. Methods Phys. Res.*, Sect. **A 554**, 20 (2005).

[24] J. Wu, Z. Huang, and P. Emma. *Phys. Rev. ST Accel. Beams* **11**, 040701 (2008).

[25] J. Qiang et al., *Nucl. Intrum. Method*, **A 457**, 11 (2001).

[26] See for instance R. W. Howckney and J. W. Eastwood, Computer Simulation using particles, Adam Higler, Bristol and New York (1989).

[27] B. E. Carsten, *Particle Accelerators*, **49**, 27 (1995).

[28] K. Flöttmann, D. Janssen, and V. Volkov, *Phys. Rev. ST Accel. Beams* **7**, 090702 (2004).

[29] William H. Press, Brian P. Flannery, Saul A. Teukolsky, William T. Vetterling, *Numerical Recipes in C*, Cambridge, UK: Cambridge University Press, second edition (1992).

[30] G. E. P. Box and M. E. Muller, *The Annals of Mathematical Statistics* **29** (2), 610 (1958).